PAPER

Check for updates

A comparative study of the effects of different TiO$_2$ supports toward CO$_2$ electrochemical reduction on CuO/TiO$_2$ electrode

Yueheng Lu, [ID] Huazhen Cao, [ID]* Shenghang Xu, Chenxi Jia [ID] and Guoqu Zheng [ID]*

CuO-based electrodes possess vast potential in the field of CO$_2$ electrochemical reduction. Meantime, TiO$_2$ supports show the advantages of being non-toxic, low-cost and having high chemical stability, which render it an ideal electrocatalytic support with CuO. However, different morphologies and structures of TiO$_2$ supports can be obtained through various methods, leading to the discrepant electrocatalytic properties of CuO/TiO$_2$. In this paper, three supports, named dense TiO$_2$, TiO$_2$ nanotube and TiO$_2$ nanofiber, were applied to synthesize CuO/TiO$_2$ electrodes by thermal decomposition, and the performances of the electrocatalysts were studied. Results show that the main product of the three electrocatalysts was ethanol, but the electrochemical efficiency and reaction characteristics are obviously different. The liquid product of CuO/Dense TiO$_2$ is pure ethanol, however, the current efficiency is rather low owing to the higher resistance of the TiO$_2$ film. CuO/TiO$_2$ nanotube shows high conductivity and ethanol can be synthesized at low overpotential with high current efficiency, but the gas products cannot be restricted. CuO/TiO$_2$ nanofiber has a larger specific surface area and more active sites, which is beneficial for CO$_2$ reduction, and the hydrogen evolution reaction can be evidently restricted. The yield of ethanol reaches up to 6.4 µmol cm^{-2} at −1.1 V (*vs.* SCE) after 5 h.

1. Introduction

CO$_2$ can be converted to chemicals with high energy density through reduction reaction, such as methanol and ethanol, and the reaction can be achieved at room temperature and atmospheric pressure. The electrocatalytic reduction reaction is expected to become a feasible way to sustainably transform the waste CO$_2$ stream into value-added low-carbon fuels, which is of great significance for energy conversion and CO$_2$ emission reduction.[1,2] However, significant competition between CO$_2$ reduction and hydrogen evolution in aqueous solution occurs, leading to the low efficiency and product selectivity.[3,4] Therefore, the application of CO$_2$ reduction is rather limited.

In recent decades, numerous trials have been made to explore electrodes with distinguished performance for CO$_2$ electrochemical reduction, including metals,[5–8] metal oxides[9–11] and metal complexes.[12–15] Herein, CuO, as a relatively low-cost and earth abundant metal oxide, possesses a unique capacity to produce hydrocarbons through a multiple protons and electrons transfer pathway, which renders it an electrocatalytic reduction electrode material with large-scale application potential.[16–18] However, CuO electrodes have a high overpotential and poor selectivity to the products, and are usually

applied with a support.[19] As an n-type semiconductor material, TiO$_2$ is one of the widely used photocatalyst and electrocatalyst supports due to its advantages of non-toxicity, low cost and high chemical stability.[20–22] Importantly, during the CO$_2$ reduction reaction, a TiO$_2$ support can help to adsorb CO$_2$ and thereby facilitate the electrocatalytic reduction.[23] Many researchers have been focused on the preparation of CuO/TiO$_2$ electrodes applied in the field of photocatalytic reduction of CO$_2$ and hydrogen production.[24–27] The morphology and structure of TiO$_2$ supports are various through different preparation methods, which in turn obviously influences the electrocatalytic performance. The combination of n-type TiO$_2$ with the p-type CuO semiconductor[28] can form a heterojunction, which has unidirectional conductivity, and it can facilitate the intramolecular electron transfer.[29,30] However, the research about the morphology and structure of the TiO$_2$ support on the electrocatalytic properties of CuO/TiO$_2$ electrodes is rather scarce.

In this paper, three TiO$_2$ supports with different morphologies were fabricated, and CuO particles were deposited on the surface of TiO$_2$ support by thermal decomposition method. Through linear sweep voltammetry (LSV) and cyclic voltammetry (CV) method, the product selectivity, stability and catalytic efficiency of these CuO/TiO$_2$ electrodes were studied in detail, and the mechanism of TiO$_2$ support morphology on catalytic behavior was revealed.

College of Materials Science and Engineering, Zhejiang University of Technology, Hangzhou 310014, China. E-mail: caohz@zjut.edu.cn; zhenggq@zjut.edu.cn

2. Experimental

2.1 Reagents

Pure Ti sheet (99.99%) was purchased from Baoji LiTai Co., Ltd. Hydrofluoric acid (HF, 40%), absolute ethanol (CH_3CH_2OH, 99.7%), methanol (CH_3OH, 99.5%), sodium hydroxide (NaOH, 96%), hydrochloric acid (HCl, 37%) and anhydrous sodium sulfate (Na_2SO_4, 99%) were purchased from Sinopharm Reagent Co., Ltd. Chromium trioxide (CrO_3, 99%), formic acid (HCOOH, 99%), copper nitrate ($Cu(NO_3)_2 \cdot 3H_2O$, 99%) and sodium bicarbonate ($NaHCO_3$, 98%) were purchased from Macklin Co., Ltd. 1-Butyl-3-methylimidazolium hexafluorophosphate ($C_8H_{15}N_2PF_6$, 99%) was purchased from Lanzhou Greenchem ILs.

2.2 Preparation of TiO₂ supports with different morphology

The pure titanium substrates were grinded and polished, and then cleaned with deionized water and ethanol sequentially. The chemical polish process was conducted in an aqueous solution of chromium trioxide hydrofluoric acid (4% HF and 7.5% CrO_3) at 50 °C for 20 min. Afterwards, the titanium substrates were sealed by PTFE raw tape and sealant, and only one side of substrate is exposed.

Dense TiO_2 was obtained by anodizing in an ionic liquid (1-butyl-3-methylimidazolium hexafluorophosphate). The negative electrode is platinum and the anodic oxidation reaction is applied at a voltage of 8 V and 10 °C for 20 min.

TiO_2 nanotubes (TNTs) were obtained by anodic oxidation in 1 wt% hydrofluoric acid aqueous solution. The negative electrode is graphite and the anodic oxidation reaction is applied at a voltage of 20 V and 25 °C for 20 min.

TiO_2 nanofibers (TiO_2NFs) were fabricated by putting Ti substrate in 10 M NaOH aqueous solution at 130 °C for 4 h through hydro-thermal method. Then, the Ti substrate was transferred to 0.1 M HCl aqueous solution for ion exchange for 12 h. Afterwards, the above electrodes were calcined in air at 450 °C for 2 h.

2.3 Preparation of TiO₂-supported CuO electrodes

The copper nitrate aqueous solution of 1.66 M was spread on the surface of TiO_2 carriers. Then, the samples were placed in
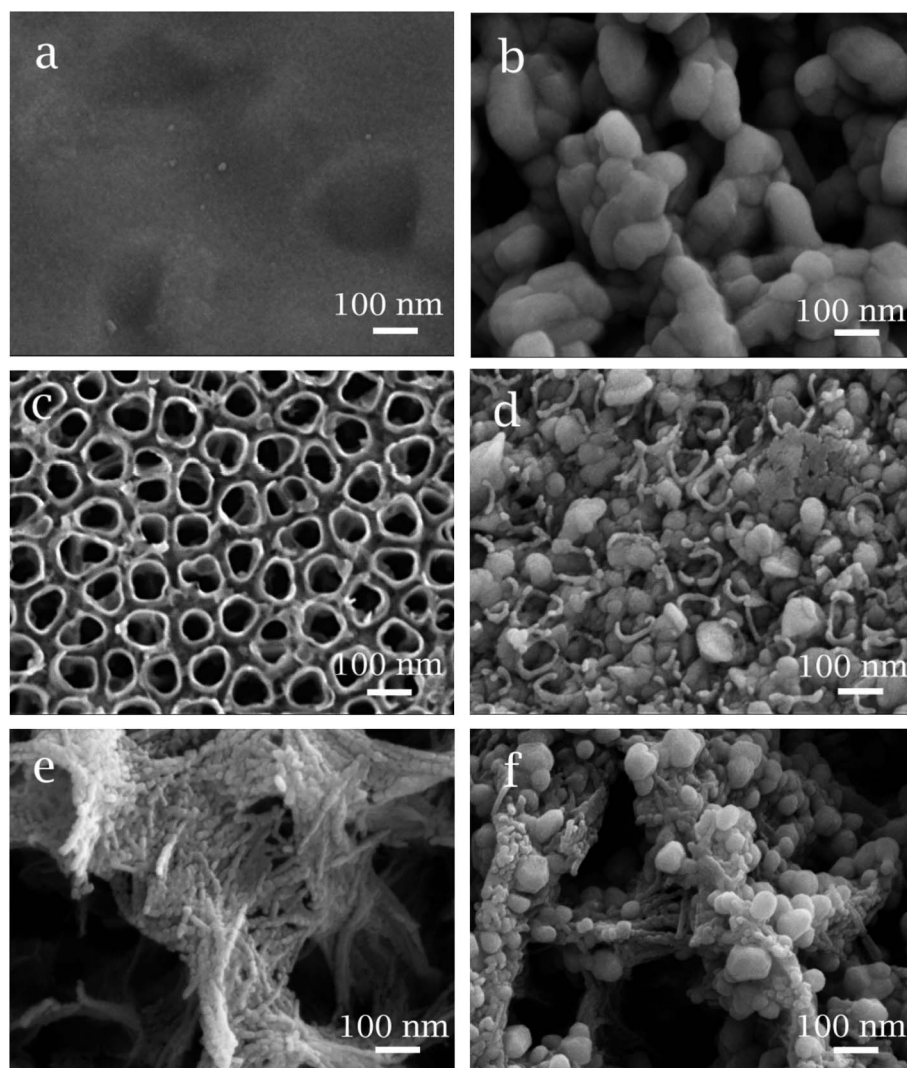

Fig. 1 SEM images of (a) dense TiO_2, (b) CuO/Dense TiO_2, (c) TNTs, (d) CuO/TNTs, (e) TiO_2NFs and (f) CuO/TiO_2NFs.

a vacuum bottle and the excess solution on the surface was removed through centrifugation. Subsequently, all samples were calcined in air at 450 °C for 20 min. The above operations were repeated until the coating weight reaches 3 mg cm^{-2}.

2.4 Characterization and electrochemical reduction tests

The composition and crystal structure of those electrodes were conducted by an X-ray diffraction (XRD, Panalytical X'Pert PRO) at 40 kV and 40 mA with a scan speed of 10° min^{-1}. The morphology and microstructure of electrodes were characterized by a field emission scanning electron microscopy (SEM, Vega3) and a transmission electron microscopy (TEM, Nano Nova 450) equipped with an energy dispersive X-ray (EDX) spectrometer.

The electrochemical experiments were investigated by a CHI660C electrochemical workstation at 25 °C water bath. A platinum foil (2 × 2 cm^2) and a saturated calomel electrode (SCE) were used as counter electrode and reference electrode, respectively. Linear sweep voltammetry (LSV) was researched in 0.1 M Na$_2$SO$_4$ solution with a scanning rate of 50 mV s^{-1} in the potential range between 0 and −1.3 V (*vs.* SCE). The electrical double-layer capacitance (C_{dl}) was measured in 0.5 M Na$_2$SO$_4$ solution to characterize electrochemical surface area (ECSA). Prior to tests, CO$_2$ or N$_2$ was bubbled into aqueous solution for 20 minutes. And the electrodes were sealed with sealant to make the exposed area 1 × 1 cm^2.

2.5 Products analysis

The reduction experiment was carried out in an 80 mL 0.1 M NaHCO$_3$ solution for 5 h. The process is conducted at a constant
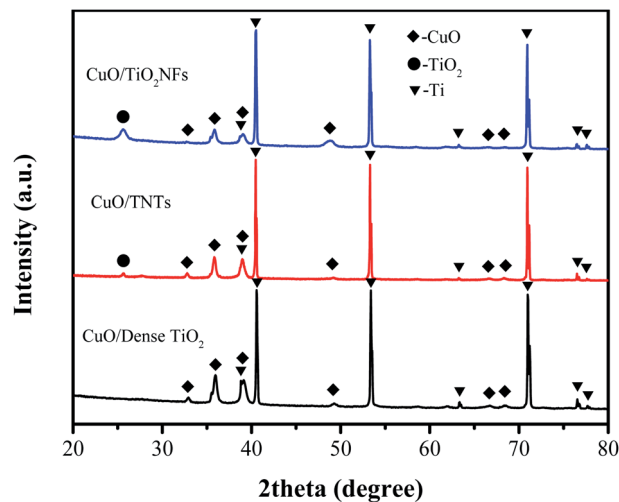

Fig. 3 XRD patterns of CuO/Dense TiO$_2$, CuO/TNTs and CuO/TiO$_2$NFs.

temperature of 25 °C. Liquid phase products were quantitatively characterized by headspace gas chromatograph (GC-G5, Purkinje, China) equipped with DB-WAX column and flame ionization detector (FID).

3. Results and discussion

3.1 Microstructure of CuO/TiO$_2$ electrodes

Fig. 1 shows the SEM morphologies of three CuO/TiO$_2$ electrodes. The surface of dense TiO$_2$ (Fig. 1a) support is gully-like.
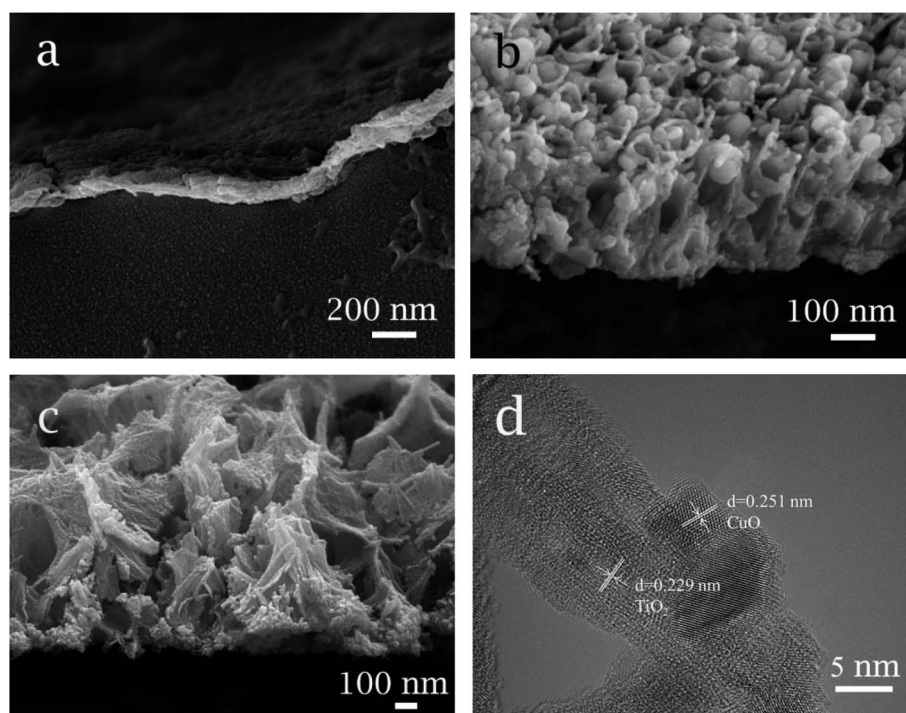

Fig. 2 Cross-sectional SEM images of electrode: (a) dense TiO$_2$, (b) CuO/TNTs, (c) TiO$_2$NFs, (d) HRTEM image of CuO/TiO$_2$NFs.
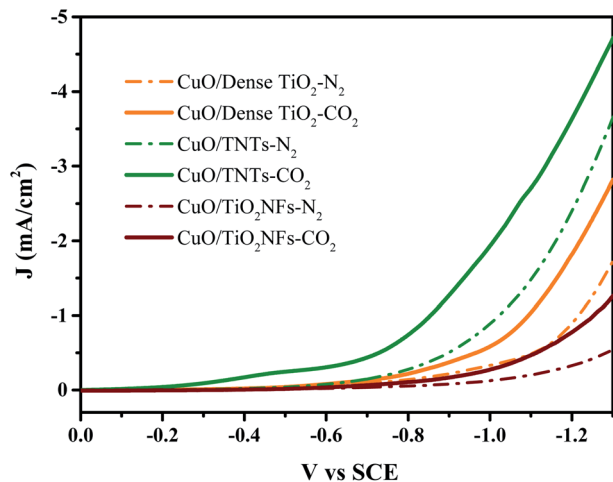
Fig. 4 LSV results of CuO/Dense TiO$_2$, CuO/TNTs and CuO/TiO$_2$NFs in 0.1 M Na$_2$SO$_4$ saturated with N$_2$ or CO$_2$.

After thermal decomposition process, CuO particles of about 100 nm are gathered on the surface of TiO$_2$, as shown in Fig. 1b. Fig. 1c shows the regularly arranged TiO$_2$ nanotube with an inner diameter of about 80 nm and a wall thickness of about 10 nm. The CuO particles are tightly packed inside and inbetween nanotubes, as shown in Fig. 1d. The particle sizes of CuO inside and inbetween nanotubes is about 40 and 100 nm, respectively. The TiO$_2$ nanofiber support shows a typical

network-like structure (Fig. 1e) and CuO particles are tightly attached on the surface of TiO$_2$ nanofiber with the size of about 40 nm (Fig. 1f).

Fig. 2a shows the SEM image of cross-section of dense TiO$_2$ support. It can be seen that the connection between TiO$_2$ and matrix is well. However, obvious cracks can be seen inside the TiO$_2$ support, which are attributed to the occurrence of interior stress during thermal decomposition process. The cross-section of CuO/TiO$_2$ nanotube electrode demonstrates the well connection between nanotube and matrix, as shown in Fig. 2b. Besides, the length of nanotube is about 300 nm and CuO particles can be deposited inside the nanotube. The cross-section of TiO$_2$ network-like structure is presented in Fig. 2c, and the thickness of TiO$_2$ network is about 500 nm. In Fig. 2d, the HRTEM image shows the lattice fringes of TiO$_2$ and CuO. The fringes with a spacing of 0.251 nm match the (−1 1 1) crystal plane of CuO, and the fringes with a spacing of 0.229 nm match the (1 1 2) crystal plane of anatase TiO$_2$.

Phase composition of different CuO/TiO$_2$ electrodes were analyzed by XRD, as shown in Fig. 3. Due to the thin film of CuO/TiO$_2$, the peaks of Ti matrix can be obviously observed (JCPDS card 01-1198) at 2θ = 40.17, 53.00 and 70.66°. The peaks of anatase TiO$_2$ (JCPDS card 75-1537) can be detected at 2θ = 25.7° in CuO/TNTs and CuO/TiO$_2$NFs, corresponding to (1 0 1) crystal plane. However, the peaks of anatase TiO$_2$ cannot be detected in CuO/Dense TiO$_2$ electrode, which is attributed to the limited thickness of TiO$_2$ layer. The peaks of CuO (JCPDS card 65-2309) can be seen in all electrodes at 32.6, 35.6, 38.8,
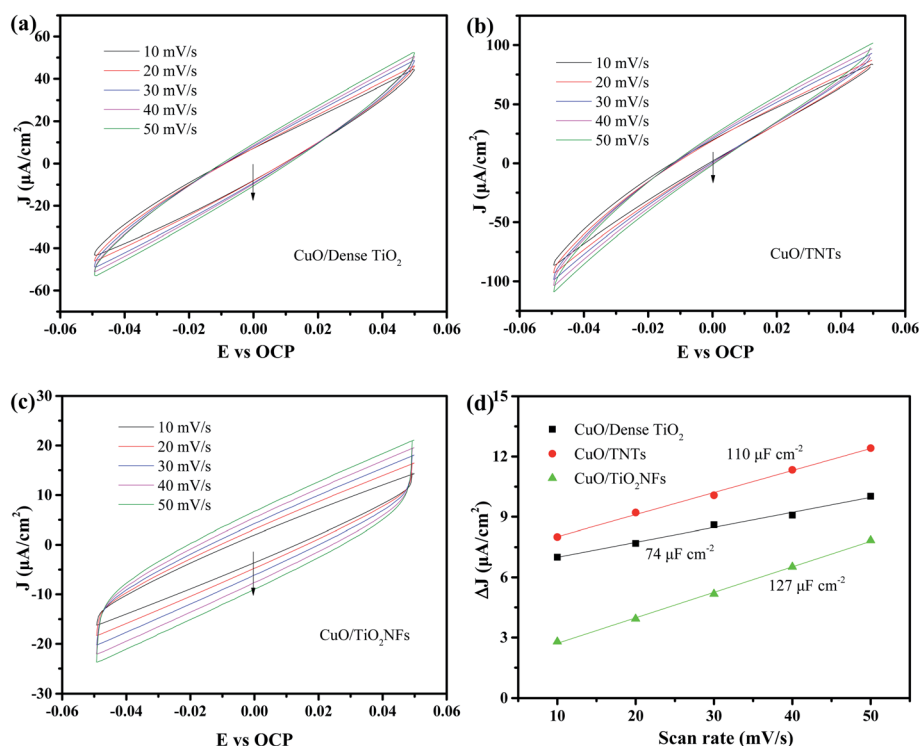

Fig. 5 CV curves of (a) CuO/Dense TiO$_2$, (b) CuO/TNTs, (c) CuO/TiO$_2$NFs in 0.5 M Na$_2$SO$_4$ aqueous solution. (d) Average value of anode and cathode current density ($\Delta j = (j_a − j_c)/2$) around the open circuit potential against the scan rate for CuO/Dense TiO$_2$, CuO/TNTs and CuO/TiO$_2$NFs, respectively.

48.9, 66.6 and 68.1°, corresponding to (1 1 0) (−1 1 1), (1 1 1) (−2 0 2), (−3 1 1) and (1 1 3) planes, respectively.

3.2 Electrocatalytic properties

Fig. 4 reveals the LSV curves of CuO/Dense TiO_2, CuO/TNTs and CuO/TiO_2NFs in 0.1 M Na_2SO_4. The dotted line represents the current density under N_2 saturated atmosphere while the solid line shows the current density under CO_2 saturated atmosphere. The deviation between the solid line and the dashed line can be regarded as the reaction current of CO_2 reduction (I_{CO_2}) approximately. The three electrodes all showed catalytic abilities for CO_2 reduction, but the overpotentials on different electrodes are much different. Specifically, the I_{CO_2} on CuO/TNTs is nearly 0.2 mA cm^{-2} at −0.5 V (*vs.* SCE). While for the case of CuO/Dense TiO_2 and CuO/TiO_2NFs electrodes, the CO_2 reduction begins at −0.6 V and −0.7 V, respectively. The different overpotentials on different electrodes are mainly related with the distinctive film resistances. For example, the dense TiO_2 layer is only about 100 nm, while the TiO_2NFs layer is nearly 1 μm. As a result, the current of CuO/Dense TiO_2 is larger than that of CuO/TiO_2NFs. It is also observed that the hydrogen evolution reaction is evidently inhibited on CuO/TiO_2NFs or CuO/TNTs.

The electrical double layer capacitance is the most commonly used method to determine the electrochemically surface area (ECSA).[31–33] Fig. 5a–c shows the CV curves of the three electrodes near open circuit potential by different sweep speeds. It can be considered that only non-Faraday charge and discharge occur in this range. The average value of anode and cathode current under the open circuit potential is selected as the electric double layer capacitance current i_C. It can be demonstrated that the double layer capacitance of CuO/Dense TiO_2, CuO/TNTs and CuO/TiO_2NFs electrode is 74, 110 and 127 μF cm^{-2} (Fig. 5d), respectively, which shows that the CuO/TiO_2NFs electrode possesses the highest ESCA and largest number of active sites.[34,35]

3.3 Electrochemical reduction of CO_2

Fig. 6a–c shows the liquid product yield and Faraday efficiency of CuO/Dense TiO_2, CuO/TNTs and CuO/TiO_2NFs after electrochemical reduction of CO_2 for 5 h. Faraday efficiency (EF) can be calculated by the following formula:

$$EF = \sum \frac{znF}{Q} \tag{1}$$

where z is the number of necessary electrons for product, 2 for formic acid, 6 for methanol, and 12 for ethanol; n is the molar number of products; F is the Faraday constant and Q is the total charge.

Fig. 7 is the gas chromatography analysis of liquid product obtained by three electrodes through electrochemical reduction of CO_2 at different potential (*vs.* SCE). The retention times of methanol and ethanol are at 3.03 min and 3.25 min, respectively. Besides, the retention time of formic appears at 2.52 min
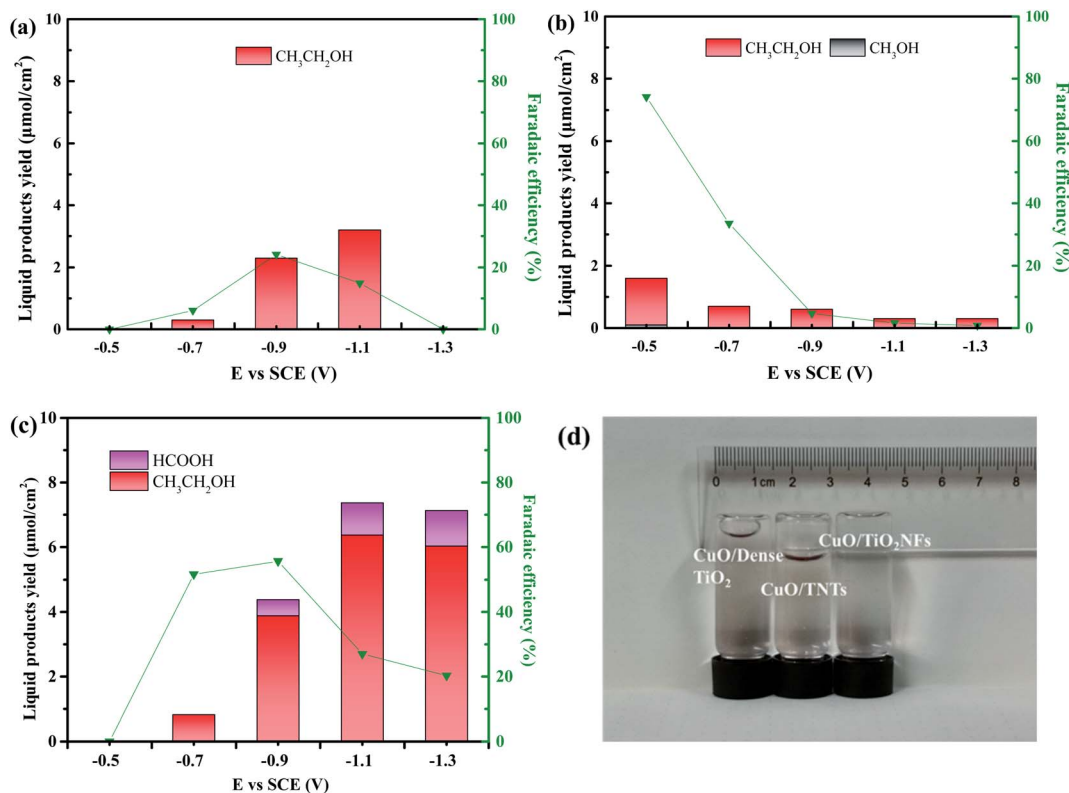

Fig. 6 The yield of liquid products and faradaic efficiency at different external voltage of (a) CuO/Dense TiO_2, (b) CuO/TNTs and (c) CuO/TiO_2NFs for 5 h. (d) The optical image of gas products of the three electrodes at −0.9 V (*vs.* SCE) for 5 h.
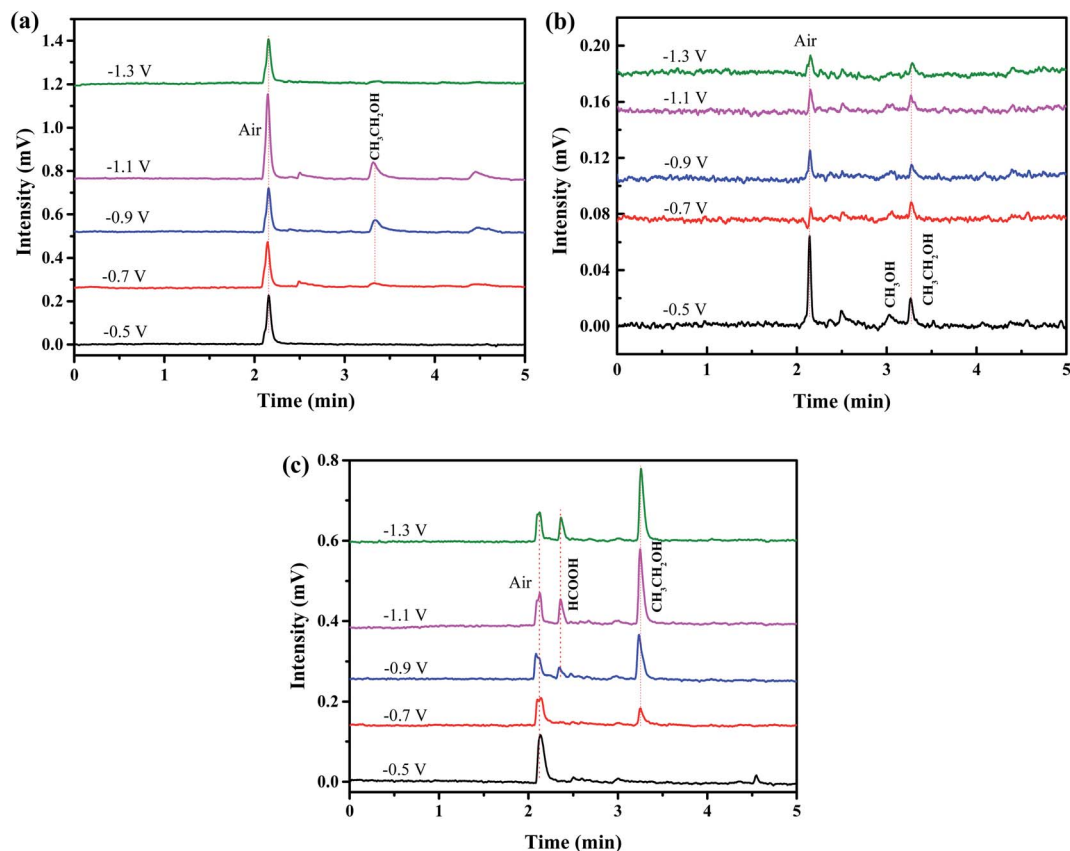
Fig. 7 Liquid products produced by different electrodes: (a) CuO/Dense TiO₂, (b) CuO/TNTs and (c) CuO/TiO₂NFs.

while that of air is at 2.12 min. It can be demonstrated that only gas and ethanol can be generated by using CuO/Dense TiO₂ electrode. A very small amount of methanol is generated by CuO/TNTs electrode while a little formic can be detected by CuO/TiO₂NFs electrode. By contrast, the yield of ethanol is pretty higher by CuO/TiO₂NFs electrode than those by CuO/Dense TiO₂ and CuO/TNTs electrodes.

Fig. 6 and 7 indicate that the liquid products by CuO/Dense TiO₂, CuO/TNTs and CuO/TiO₂NFs have high selectivity, and the main product is ethanol. With increasing the bias voltage, the yield of liquid products by CuO/Dense TiO₂ electrode gradually improves. The maximum ethanol production of 3.2 μmol cm^{-2} can be obtained when the bias voltage is around −1.1 V. As for the CuO/TNTs electrode, the Faraday efficiency reaches up to 74.2% at −0.5 V, and the yield of ethanol is 1.6 μmol cm^{-2} with small amount of methanol. With increasing the bias voltage, the yield of liquid products and Faraday efficiency decrease evidently. As regards the CuO/TiO₂NFs electrode, the improvement of bias voltage leads to the increased formation of liquid products. The yield of ethanol and formic acid reaches up to 6.4 μmol cm^{-2} and 1.0 μmol cm^{-2} at −1.1 V, respectively.

Fig. 8 shows the time−current curves of three electrodes for electrochemical reduction of CO₂ at −0.9 V, reaches a maximum value and then decreases to a stable value. Many literatures has proved that during CO₂ electroreduction process, less of the charge could be attributed to the reduction of CuO to

Cu₂O and potentially Cu.[36] Our previous studies also confirmed the existence of Cu after CuO/TNTs catalyst was applied in CO₂ reduction.[37] So a modest increase in current was observed during the initial stage of CO₂ reduction process. However, the Cu film exhibited a lower activity compared with the oxide film, and the gas bubbled at the interface of electrode blocks the
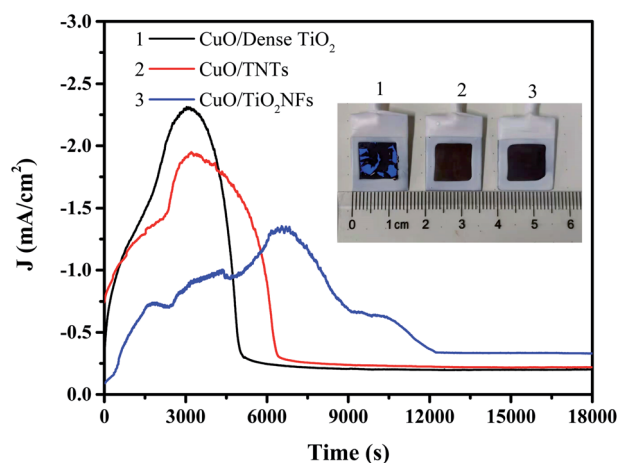

Fig. 8 Current−time curve of CuO/Dense TiO₂, CuO/TNTs and CuO/TiO₂NFs in 0.1 M NaHCO₃ saturated with CO₂ at −0.9 V (vs. SCE) for 5 h, and the inset optical image shows the surface condition after electrochemical reduction.

available catalytic sites, which both caused the current decay with prolonging time. As a result, reduction peaks were observed in the chronoamperometry curves of CuO catalysts during the initial stage of CO_2 reduction. This result was consistent with the studies by Yeo et al.[38] Besides, it is noted that the maximum current of CuO/Dense TiO_2, CuO/TNTs occurs at 3000 s while that of CuO/TiO_2NFs is 7000 s. The stable current density of CuO/Dense TiO_2 and CuO/TNTs is 0.22 and 0.20 mA cm^{-2}, respectively, and CuO/TiO_2NFs shows a higher stable current density of 0.33 mA cm^{-2}. The longer peak time and the higher stable current both indicate that CuO/TiO_2NFs may have a higher efficiency for the generation of CO_2 reduction products. After CO_2 electrochemical reduction for 18 000 s, the surface of CuO/Dense TiO_2 electrode cracks and strips while those of CuO/TiO_2TNTs and CuO/TiO_2NFs are relatively stable.

It is well-accepted that the electrochemical reduction efficiency is tightly related to the surface roughness of CuO/TiO_2 heterojunction, the stability of TiO_2 supports, ESCA and the activity of hydrogen evolution reaction. The current density of dense TiO_2 support is high, however, the electric resistance of TiO_2 layer is rather tremendous, leading to the low current efficiency. Besides, owing to the relatively low specific surface area, the contact area between CO_2 and electrode is limited, leading to the inhibition of electrochemical reduction of CO_2 and the promotion of hydrogen evolution reaction. Meanwhile, as mentioned above, some cracks generate during the fabricating process, and the bubbles produced by hydrogen evolution reaction will accelerate the generation and peeling of cracks, which leads to the instability of CuO/Dense TiO_2. In the CuO/TNTs electrode, the TiO_2 nanotubes combine well with Ti matrix and CuO particles. The nanotubes have excellent electrical conductivity, so the current density is extremely high during electrochemical reduction process. Besides, the CuO/TNTs electrode is more favorable for reduction reaction of CO_2, and the synthesized ethanol shows excellent purity and high current efficiency. However, with the increase of bias voltage, the hydrogen evolution reaction gradually dominates and inhibits the formation of ethanol. Besides, the formed gas on the electrode hinders the contact between electrode and CO_2, which can also suppress the reduction reaction of CO_2. Therefore, the yield of gaseous products by CuO/TNTs electrode is highest among three electrodes, and the synthesized ethanol decreases with the increase of bias voltage. CuO/TiO_2NFs electrode has the highest ethanol yield and best stability, which is caused by the distinctive surface structure. CuO/TiO_2NFs has a larger specific surface area. Studies have shown that rough or high-surface-area surfaces exhibit improved hydrocarbon selectivity.[39] This is typically attributed to the increased population of undercoordinated sites. In addition, high specific surface area catalysts also tend to suppress hydrogen evolution due to the poorer mass transport in porous systems. Many papers have been published regarding CO_2 reduction on copper-derived oxides,[40–42] but the key factors responsible for the improved selectivity and activity are still debated. However, it's reported that increased stabilization of the CO_2 anionic adsorbate ($CO_2^{\cdot-}$) by grain boundaries as well as the presence of (sub)surface oxygen play a role.[43,44] And CuO/TiO_2NFs shows more grain boundaries compared with the other two electrodes. It is generally believed that during the CO_2 reduction process, the copper oxide on the surface of these electrodes should be completely converted to metallic Cu. However, a residual oxide layer was shown to remain present on the surface during the catalysis process, and it was proposed that the surface oxide layer still serves as key reaction sites for catalysis.[45]

4. Conclusions

Three TiO_2 supports with different morphologies are successfully fabricated through anodic oxidation and hydrothermally methods, and the CuO particles are deposited by thermal decomposition. The CuO/Dense TiO_2, CuO/TNTs and CuO/TiO_2NFs show relatively good selectivity and the main product is ethanol. The liquid product of the CuO/Dense TiO_2 electrode is pure ethanol, but the current efficiency is poor. Ethanol can be synthesized by CuO/TNTs at low overpotential with high current efficiency, but the yield of gaseous products is redundant. CuO/TiO_2NFs shows rougher surface of CuO/TiO_2 heterojunction, representing best property of CO_2 reduction reaction. When the bias voltage is at −1.1 V, the yield of ethanol of CuO/TNTs electrode reaches 6.4 μmol cm^2 after 5 h.

Conflicts of interest

There are no conflicts to declare.

Acknowledgements

References

1 H. Ge, Z. Gu, P. Han, H. Shen, A. M. Al-Enizi, L. Zhang and G. Zheng, *J. Colloid Interface Sci.*, 2018, **531**, 564–569.

2 R. J. Lim, M. Xie, M. A. Sk, J.-M. Lee, A. Fisher, X. Wang and K. H. Lim, *Catal. Today*, 2014, **233**, 169–180.

3 H. Zhong, K. Fujii and Y. Nakano, *J. Electrochem. Soc.*, 2017, **164**, F923–F927.

4 M. Zhao, H. Tang, Q. Yang, Y. Gu, H. Zhu, S. Yan and Z. Zou, *ACS Appl. Mater. Interfaces*, 2020, **12**, 4565–4571.

5 J. He, N. J. J. Johnson, A. Huang and C. P. Berlinguette, *ChemSusChem*, 2018, **11**, 48–57.

6 A. H. M. da Silva, S. J. Raaijman, C. S. Santana, J. M. Assaf, J. F. Gomes and M. T. M. Koper, *J. Electroanal. Chem.*, 2021, **880**, 114750.

7 M. Azuma, *J. Electrochem. Soc.*, 1990, **137**, 7–26.

8 X. Yang, J. Cheng, B. Fang, X. Xuan, N. Liu, X. Yang and J. Zhou, *Nanoscale*, 2020, **12**, 18437–18445.

9 S.-Y. Zhang, H.-L. Zhu and Y.-Q. Zheng, *Electrochim. Acta*, 2019, **299**, 281–288.

10 N. Ullah, I. Ali, M. Jansen and S. Omanovic, *Can. J. Chem. Eng.*, 2015, **93**, 55–62.

11 A. H. M. da Silva, S. J. Raaijman, C. S. Santana, J. M. Assaf, J. F. Gomes and M. T. M. Koper, *J. Electroanal. Chem.*, 2021, **880**, 114750.

12 Q. Wang, Y. Zhang, H. Lin and J. Zhu, *Chem.–Eur. J.*, 2019, **25**, 14026–14035.

13 J. Albo, D. Vallejo, G. Beobide, O. Castillo, P. Castaño and A. Irabien, *ChemSusChem*, 2017, **9**, 1–11.

14 G. Liao, J. Fang, Q. Li, S. Li, Z. Xu and B. Fang, *Nanoscale*, 2019, **11**, 7062–7096.

15 J.-H. Liu, L.-M. Yang and E. Ganz, *RSC Adv.*, 2019, **9**, 27710–27719.

16 J. Xie, Y. Huang and H. Yu, *Front. Environ. Sci. Eng.*, 2014, **9**, 861–866.

17 Y. Lum and J. W. Ager, *Nat. Catal.*, 2018, **2**, 86–93.

18 L. Mandal, K. R. Yang, M. R. Motapothula, D. Ren, P. Lobaccaro, A. Patra, M. Sherburne, V. S. Batista, B. S. Yeo, J. W. Ager, J. Martin and T. Venkatesan, *ACS Appl. Mater. Interfaces*, 2018, **10**, 8574–8584.

19 T. Moller, F. Scholten, T. N. Thanh, I. Sinev, J. Timoshenko, X. Wang, Z. Jovanov, M. Gliech, B. Roldan Cuenya, A. S. Varela and P. Strasser, *Angew. Chem., Int. Ed.*, 2020, **59**, 17974–17983.

20 K. Kočí, K. Matějů, L. Obalová, S. Krejčíková, Z. Lacný, D. Plachá, L. Čapek, A. Hospodková and O. Šolcová, *Appl. Catal., B*, 2010, **96**, 239–244.

21 O. Ola and M. M. Maroto-Valer, *J. Photochem. Photobiol., C*, 2015, **24**, 16–42.

22 M. Niu, D. Cheng and D. Cao, *J. Phys. Chem. C*, 2013, **117**, 15911–15917.

23 G. K. Ramesha, J. F. Brennecke and P. V. Kamat, *ACS Catal.*, 2014, **4**, 3249–3254.

24 J. Yuan, J.-J. Zhang, M.-P. Yang, W.-J. Meng, H. Wang and J.-X. Lu, *Catalysts*, 2018, **8**, 171.

25 S. Qin, F. Xin, Y. Liu, X. Yin and W. Ma, *J. Colloid Interface Sci.*, 2011, **356**, 257–261.

26 P. Khemthong, P. Photai and N. Grisdanurak, *Int. J. Hydrogen Energy*, 2013, **38**, 15992–16001.

27 T. N. Ravishankar, M. d. O. Vaz and S. R. Teixeira, *New J. Chem.*, 2020, **44**, 1888–1904.

28 S. M. Park, A. Razzaq, Y. H. Park, S. Sorcar, Y. Park, C. A. Grimes and S. I. In, *ACS Omega*, 2016, **1**, 868–875.

29 Q. Wu, M. J. Mao, Q. J. Wu, J. Liang, Y. B. Huang and R. Cao, *Small*, 2020, e2004933.

30 D.-D. Ma, S.-G. Han, C. Cao, W. Wei, X. Li, B. Chen, X.-T. Wu and Q.-L. Zhu, *Energy Environ. Sci.*, 2021, **14**, 1544–1552.

31 D. Voiry, M. Chhowalla, Y. Gogotsi, N. A. Kotov, Y. Li, R. M. Penner, R. E. Schaak and P. S. Weiss, *ACS Nano*, 2018, **12**, 9635–9638.

32 X. Lu, R. Liu, Q. Wang and C. Xu, *ACS Appl. Mater. Interfaces*, 2019, **11**, 40014–40021.

33 L. Xu, Q. Jiang, Z. Xiao, X. Li, J. Huo, S. Wang and L. Dai, *Angew. Chem., Int. Ed.*, 2016, **55**, 5277–5281.

34 W. Hao, R. Wu, R. Zhang, Y. Ha, Z. Chen, L. Wang, Y. Yang, X. Ma, D. Sun, F. Fang and Y. Guo, *Adv. Energy Mater.*, 2018, **8**, 1801372.

35 H. Wu, K. Yin, W. Qi, X. Zhou, J. He, J. Li, Y. Liu, J. He, S. Gong and Y. Li, *ChemSusChem*, 2019, **12**, 2773–2779.

36 L. Zhang, H. Cao, Y. Lu, H. Zhang, G. Hou, Y. Tang and G. Zheng, *J. Solid State Electrochem.*, 2019, **24**, 447–459.

37 L. Wang, K. Gupta, J. Goodall, J. A. Darr and K. B. Holt, *Faraday Discuss.*, 2016, **197**, 517–532.

38 D. Ren, Y. Deng, A. D. Handoko, C. S. Chen, S. Malkhandi and B. S. Yeo, *ACS Catal.*, 2015, **5**, 2814–2821.

39 W. Tang, A. A. Peterson, A. S. Varela, Z. P. Jovanov, L. Bech, W. J. Durand, S. Dahl, J. K. Norskov and I. Chorkendorff, *Phys. Chem. Chem. Phys.*, 2012, **14**, 76–81.

40 C. W. Li, J. Ciston and M. W. Kanan, *Nature*, 2014, **508**, 504–507.

41 A. Dutta, M. Rahaman, N. C. Luedi, M. Mohos and P. Broekmann, *ACS Catal.*, 2016, **6**, 3804–3814.

42 R. Kas, R. Kortlever, A. Milbrat, M. T. Koper, G. Mul and J. Baltrusaitis, *Phys. Chem. Chem. Phys.*, 2014, **16**, 12194–12201.

43 X. Feng, K. Jiang, S. Fan and M. W. Kanan, *ACS Cent. Sci.*, 2016, **2**, 169–174.

44 A. Eilert, F. Cavalca, F. S. Roberts, J. Osterwalder, C. Liu, M. Favaro, E. J. Crumlin, H. Ogasawara, D. Friebel, L. G. Pettersson and A. Nilsson, *J. Phys. Chem. Lett.*, 2017, **8**, 285–290.

45 D. Kim, S. Lee, J. D. Ocon, B. Jeong, J. K. Lee and J. Lee, *Phys. Chem. Chem. Phys.*, 2015, **17**, 824–830.